OPTICS

Breaking the limitation of polarization multiplexing in optical metasurfaces with engineered noise

Bo Xiong[1]†, Yu Liu[1]†, Yihao Xu[2]†, Lin Deng[3], Chao-Wei Chen[1], Jia-Nan Wang[1], Ruwen Peng[1]*, Yun Lai[1], Yongmin Liu[2,3]*, Mu Wang[1,4]*

Noise is usually undesired yet inevitable in science and engineering. However, by introducing the engineered noise to the precise solution of Jones matrix elements, we break the fundamental limit of polarization multiplexing capacity of metasurfaces that roots from the dimension constraints of the Jones matrix. We experimentally demonstrate up to 11 independent holographic images using a single metasurface illuminated by visible light with different polarizations. To the best of our knowledge, it is the highest capacity reported for polarization multiplexing. Combining the position multiplexing scheme, the metasurface can generate 36 distinct images, forming a holographic keyboard pattern. This discovery implies a new paradigm for high-capacity optical display, information encryption, and data storage.

Metasurfaces (*1*–*3*) provide rich degrees of freedom (DOFs) to modulate the phase (*4*, *5*), amplitude (*6*, *7*), and polarization (*8*, *9*) of light based on subwavelength structures. Compared with traditional optical devices, metasurfaces possess distinct advantages of the ultrathin thickness (*10*, *11*), high efficiency (*12*–*14*), and broadband responses (*15*–*17*). In recent years, metasurfaces have been demonstrated for wavelength multiplexing (*18*, *19*), angle multiplexing (*20*), and orbital angular momentum (OAM) multiplexing (*21*), as well as reconfigurable metadevices (*22*, *23*).

Polarization (*24*–*27*) has been explored in metasurfaces for large-capacity multiplexing technology, which can transmit information through independent channels to different desired targets. However, there exists an upper limit in the capacity of polarization multiplexing. Traditionally, two orthogonal linear polarizations (e.g., *x*- and *y*-polarized components) operate dual independent functionalities without cross-talk in a two-dimensional (2D) planar optical platform such as a metasurface (*28*, *29*). This approach relies on the diagonal elements of the Jones matrix, which is a 2 × 2 matrix representing the optical response of a metasurface. Amplitude modulation has also been introduced in polarization multiplexing. Applying Malus's law has led to the design of metadevices to encode nanoprinting and holography simultaneously in the near- and far-field, respectively (*30*, *31*). More recently, the off-diagonal elements of the Jones matrix were used as an extra degree of freedom, realizing three independent polarization channels (*32*) and achieving triple sets of printing-hologram integrations (*33*). This approach reaches the theoretical upper limit (≤3 independent channels) of polarization multiplexing capacity in 2D planar metasurfaces. This restriction applies not only to linear polarizations, but also to circular polarizations [left circular polarization (LCP) and right circular polarization (RCP)] (*34*, *35*), and even arbitrary polarizations (*36*). Although polarization multiplexing has been substantially advanced through physics-guided forward design (*37*, *38*) and data-driven inverse design based on machine learning (*39*, *40*), the fact that the number of independent channels is limited to three is a notable constraint in practical applications. Breaking this upper limit will be crucial for developing high-capacity optical displays and data storage.

We develop an approach based on noise engineering that breaks this fundamental limit. By introducing the correlated noise with least-squares estimation, new polarization channels can be created with only moderate cross-talk. To reduce the cross-talk, we further introduce the noncorrelated noise with a random distribution to push the limit of polarization multiplexing. Illuminated by the incidence with different linear polarization states, the metasurface can generate up to 11 independent holographic images at the corresponding channels. Simulation shows that the capacity could be expanded further by combining our methodology with position multiplexing or OAM multiplexing. As a proof of concept, we demonstrate 36 distinct holographic images, forming a typical keyboard pattern by simultaneously using polarization multiplexing and position multiplexing.

Design strategy for engineered noise

Our design strategy is based on approximate solutions of the Jones matrix elements with sufficient engineered noise, allowing us to overcome the constraint in the polarization multiplexing capacity of metasurfaces (Fig. 1). The unit cell of the metasurface (Fig. 1A) working in the reflective configuration consists of multiple rectangular resonators with distinct lengths (L), widths (W), and rotation angles (ϕ), each of which supports two eigen dipoles along the short and long axes (see details in supplementary note 1). The Jones matrix of the unit cell is given by $\begin{bmatrix} E_x & E_{xy} \\ E_{xy} & E_y \end{bmatrix}$, where E_x, E_{xy}, and E_y are complex numbers and represent the effective Jones matrix elements. They are determined by the parameter group $\{L_i,\ W_i, \phi_i\}$, where i indicates the serial number of rectangular resonators. In the presence of M incident light beams with different linear polarizations, the corresponding optical responses of the unit cell can be generalized to Eq. 1 (details in supplementary note 2)

$$\begin{bmatrix} O_1 \\ O_2 \\ O_3 \\ \cdots \\ O_M \end{bmatrix} = \begin{bmatrix} \cos^2\theta_1 & \sin 2\theta_1 & \sin^2\theta_1 \\ \cos^2\theta_2 & \sin 2\theta_2 & \sin^2\theta_2 \\ \cos^2\theta_3 & \sin 2\theta_3 & \sin^2\theta_3 \\ \cos^2\theta_M & \cdots \\ & \sin 2\theta_M & \sin^2\theta_M \end{bmatrix} \cdot \begin{bmatrix} E_x \\ E_{xy} \\ E_y \end{bmatrix}. \quad (1)$$

Here O_M denotes the complex reflected field at the M-th linear polarization channel along the polarization angle θ_M (with respect to the x axis). Equation 1 is a collection of nonhomogeneous linear equations that can be written as $O = A \cdot E$. According to linear algebra (*41*), Eq. 1 has a precise solution for the required Jones matrix elements only if $M \leq 3$. Therefore, the independent channels for polarization multiplexing have an upper limit of 3, consistent with the conclusion of several previous works (*33*–*36*) based on the analysis of DOFs. When $M = 4$, the fourth channel is the superposition of the first three polarization channels (see details in supplementary note 3).

We deliberately introduce noise into our system to break the polarization multiplexing limit of metasurfaces, offering new DOFs in the design space. In the first step, the introduction of correlated noise creates additional polarization channels by considering the least-squares solution (*41*) instead of the precise solution of Eq. 1. By solving such overdetermined linear equations, the correlated noise is automatically introduced. The new solution can be written as $\hat{E} = (A^T A)^{-1} A^T O$ (see details in supplementary note 4), and thus the complex outputs $\hat{O} = A \cdot \hat{E}$ (e.g., $\hat{O}_1$, $\hat{O}_2$, $\hat{O}_3$, $\hat{O}_4$ when $M = 4$) can be expressed by the solid black arrows in Fig. 1B. The dashed long arrows represent the target signals at the corresponding polarization channels, whereas the dashed short ones represent the correlated noise (defined as $\Delta O_c = |A \cdot \hat{E} - O|$). It

[1]National Laboratory of Solid State Microstructures, School of Physics, and Collaborative Innovation Center of Advanced Microstructures, Nanjing University, Nanjing, 210093, China. [2]Department of Mechanical and Industrial Engineering, Northeastern University, Boston, MA 02115, USA. [3]Department of Electrical and Computer Engineering, Northeastern University, Boston, MA 02115, USA. [4]American Physical Society, 100 Motor Pkwy, Hauppauge, NY 11788, USA.
*Corresponding author. Email: rwpeng@nju.edu.cn (R.P.); y.liu@northeastern.edu (Y.Liu); muwang@nju.edu.cn (M.W.)
†These authors contributed equally to this work.

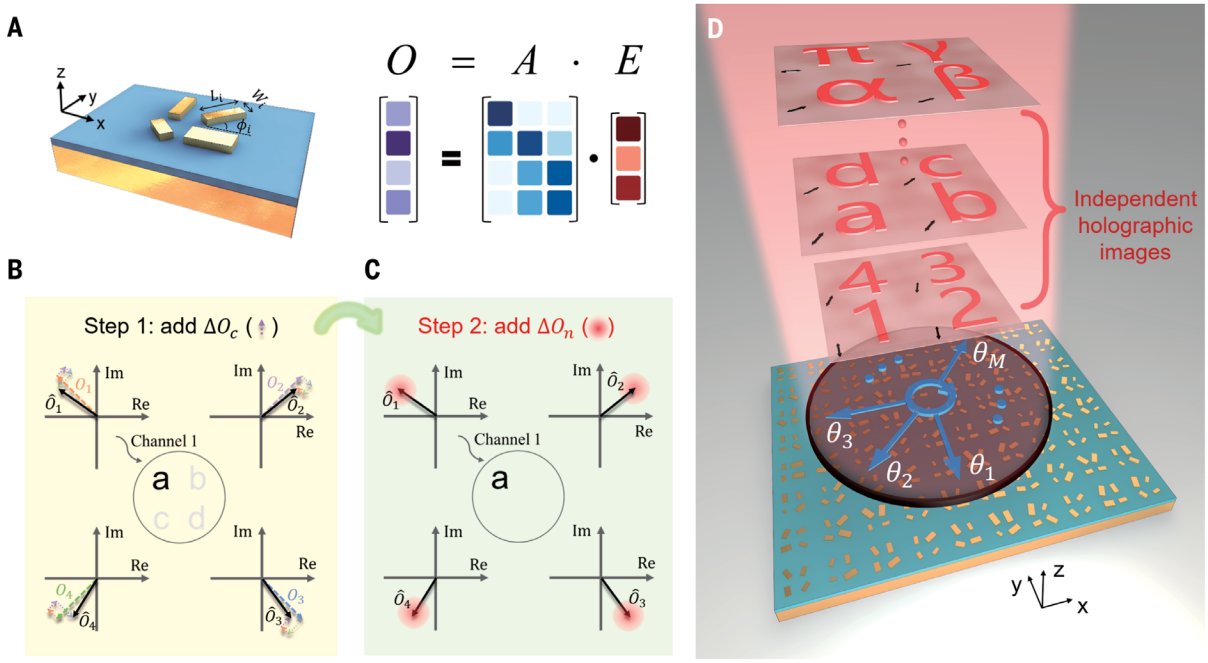

Fig. 1. Schematic of the design of polarization-multiplexed metasurface. (**A**) Designed unit cell and the corresponding response matrix. (**B**) In step 1, the least-squares solutions (solid black arrows) with the correlated noise (dashed short arrows) are introduced to create new polarization channels, where the target signals (dashed long arrows) are entirely distinct from each other. However, as shown in the inset, the solved complex outputs still have some correlations, resulting in the moderate cross-talk of holographic images. (**C**) In step 2, the random noncorrelated noise (red shadow circles) is introduced, which breaks the correlation between different channels and eliminates the cross-talk. (**D**) Schematic of the polarization-multiplexed metasurface. By changing the polarization direction of the incident light, the metasurface can generate multiple independent holographic images.

follows that the target signal of the fourth channel is entirely distinct from the other three, indicating the generation of new functionality. However, we emphasize that the correlated noise can be theoretically decomposed into the perturbations from the other channels (see details in supplementary note 4). The outputs at different polarization channels are linearly correlated, resulting in the moderate cross-talk of holographic images between different polarization channels (Fig. 1B, insets).

To eliminate such cross-talk, we proceed to the second step and add the noncorrelated noise (details shown in supplementary note 5), represented by the red shadow circles in Fig. 1C. In this case, the new solution is expressed as $\hat{E}_n = (A^T A)^{-1} A^T O + \delta E$, where each component of δE is randomly sampled from a 2D complex normal distribution $r \times N(0, I)$. Here r indicates the amplitude of the random noise, and I is the identity matrix. Then the noncorrelated noise can be written as $\Delta O_n = |A \bullet \delta E|$. Such noise is similar to the additive Gaussian noise in information theory (*42*), which mimics the effects of many random processes occurring in nature, including black body radiation from Earth and other warm objects, thermal vibrations of atoms in conductors (referred to as thermal noise), and random manufacturing error in experiments. According to the central limit theorem (*43*), the probability distribution of the mean noise produced by vast random events actually approaches a Gaussian distribution. They are typically undesirable but ultimately are beneficial in our design. As illustrated in fig. S5, when the value of r increases from 0 to 1, the correlation between the neighboring channels is gradually broken down by the noncorrelated noise, although the intensity in the target channels becomes lower. Consequently, the cross-talk between different polarization channels diminishes by selecting an appropriate value of r, realizing polarization multiplexing with a single metasurface (Fig. 1D). This result highlights that correlated and noncorrelated noise have distinct physical origins and implications. The correlated noise can be passively introduced by solving the overdetermined linear equations, which creates additional information channels with certain cross-talk. The intentionally introduced noncorrelated noise with a Gaussian noise formula substantially reduces the cross-talk, despite sacrificing the signal-to-noise ratio in the primary channels.

Testing the design strategy

We first take $M = 5$ to test our design. Figure 2A shows the calculated histogram phase distribution of ΔO_c with a mean value of ~0.22π and a standard deviation of ~0.21π. Such a noise value is relatively low in the metasurface design, close to the noise amplitude in four-level phase discretization (~0.25π). It follows that five holographic images can be generated at five polarization states (fig. S6). However, the created holographic images still contain some cross-talk from the other channels. To suppress the cross-talk, we introduce an appropriate noncorrelated noise ($r = 0.3$) with a mean value of ~0.39π and a standard deviation of ~0.28π (Fig. 2B), which is similar to the case of binary phase design. These results demonstrate that the engineered noise is within the margin of the design error. Then we design a device with multiplexed holographic images (Fig. 2D), following the iterative Fourier transform algorithm (*44*) and genetic algorithm (*45*). The final approximate solutions with engineered correlated and noncorrelated noise are fed into the genetic algorithm as complex numbers, which can search the optimized geometrical parameters for each pixel with the smallest mean square error. The genetic algorithm is critical to the design of the metasurface. By mimicking the natural processes of selection, reproduction, mutation, and crossover, the genetic algorithm is a metaheuristic algorithm that can solve global optimization problems and effectively explore the parameter space (details shown in supplementary note 6). Figure 2E presents the simulation result in which five

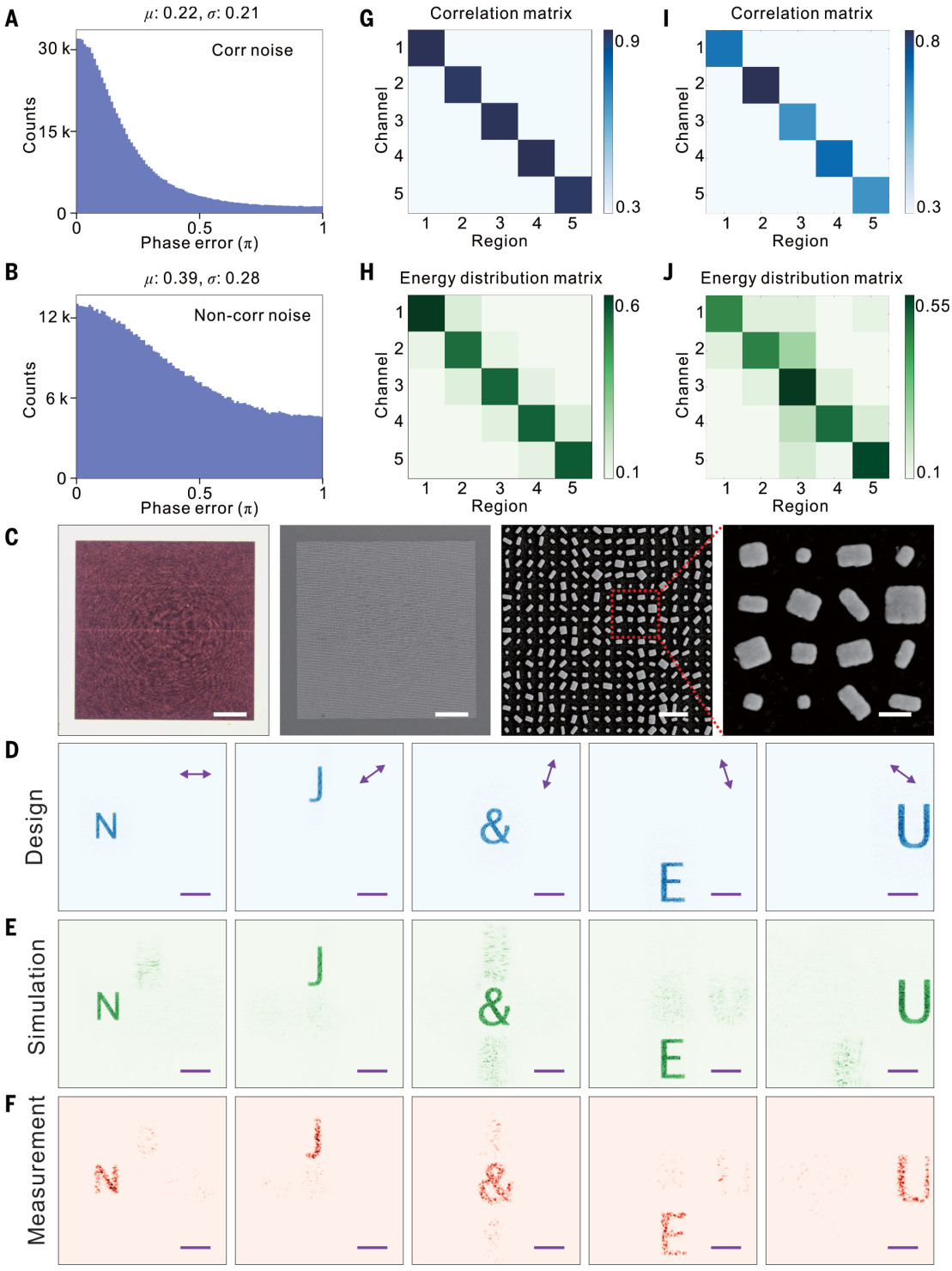

Fig. 2. Design and experimental demonstration of the five-channel polarization-multiplexed metasurface. (**A**) Calculated correlated noise distribution based on Eq. 1, which has a mean value of ~0.22π and a standard deviation of ~0.21π. (**B**) Added noncorrelated noise distribution with a mean value of 0.39π and a standard deviation of 0.28π. (**C**) Optical and SEM micrographs of the fabricated sample with different magnifications. The scale bars from left to right are 40 μm, 40 μm, 0.5 μm, and 250 nm, respectively. (**D**) Designed, (**E**) simulated, and (**F**) measured holographic images with different polarization incidences, which are marked by the purple arrows. All scale bars are 40 μm. When the incident light is polarized along 0°, 36°, 72°, 108°, and 144°, the metasurface will generate five independent holographic images, including "N", "J", "&", "E", and "U". (**G**) Calculated correlation coefficients matrix and (**H**) energy distribution matrix based on the simulation results in (E). (**I**) Measured correlation coefficients matrix and (**J**) energy distribution matrix based on the experimental results in (F), which agree well with the simulations.

independent holographic images can be generated from the same metasurface when the polarization of incident light varies. Figure 2C shows the optical and scanning electron microscopy (SEM) micrographs of the sample (220 μm by 220 μm in size) fabricated by standard electron beam lithography. The working wavelength of the metasurface is 700 nm. From the measurement results presented in Fig. 2F, we can observe that the same metasurface generates five independent holographic images—"N", "J", "&", "E", and "U"—at the corresponding polarization states (0°, 36°, 72°, 108°, 144°) (details shown in supplementary note 7).

To quantify the cross-talk between the images at different channels, we introduce the correlation coefficient, which is defined as (*46*, *47*)

$$\rho(T,R) = \frac{\mathrm{COV}(T,R)}{\sqrt{D(T)\cdot D(R)}} \qquad (2)$$

Here T and R represent the intensity distribution of the target object and reconstructed object, $\mathrm{COV}(T,R)$ is the covariance of T and R, and $D(T)$ and $D(R)$ represent the variances of T and R, respectively. According to this definition, if we consider M polarization channels, we can calculate the correlation matrix with a size of $M \times M$, in which the diagonal terms represent the target signal, whereas the non-diagonal values indicate the cross-talk. The simulated correlation coefficients of the non-diagonal terms are all below 0.3 (Fig. 2G), confirming that these polarization channels are relatively uncorrelated and hence independent. Moreover, up to 60% of the power is directed to the targeted channel (Fig. 2H). The measured correlation matrix and energy distribution matrix in Fig. 2, I and J, also agree well with the simulations. Here the fabrication error acts as an additional noncorrelated noise component that further reduces the cross-talk between the channels. These results demonstrate that by combining ΔO_c and ΔO_n, we can successfully break the constraint in the polarization

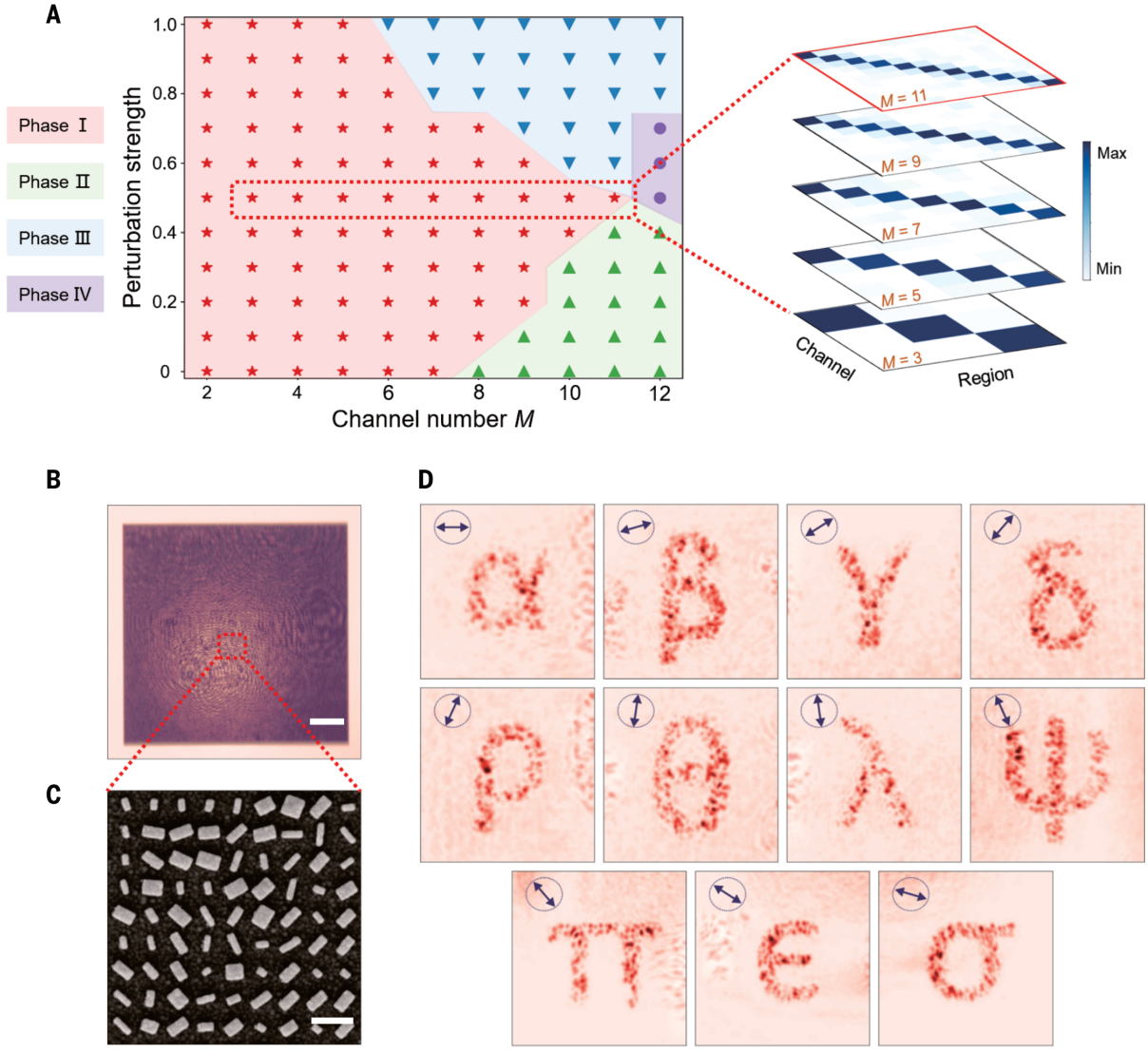

Fig. 3. Simulation and experimental demonstration of the new upper limit. (**A**) Phase diagram for polarization multiplexing in our design. Phase I represents the conditions that satisfy the threshold requirements. Phase II represents the cases in which the noncorrelated noise is so small that the nondiagonal term is more significant than 0.2, indicating that the cross-talk is rather substantial. Phase III represents the cases in which the noncorrelated noise is so large that the diagonal term is larger than 0.8, indicating that the energy in the design channel is rather weak. Phase IV indicates the scenarios where all the threshold conditions are not satisfied. The inset in the right panel shows the corresponding correlation coefficient matrices for different channel numbers from $M = 3$ to 11, all of which satisfy the threshold requirements. (**B**) Optical and (**C**) SEM micrograph of the fabricated sample for $M = 11$. The scale bars are 50 μm and 0.4 μm, respectively. (**D**) Measured holographic images at 11 linear polarization states. The arrows denote the polarization orientations.

multiplexing capacity of metasurfaces and realize the polarization-multiplexed metasurface with an independent channel number larger than 3.

The upper limit for channel number

We calculate the phase diagram for polarization multiplexing (Fig. 3). The correlated noise distributions from $M = 2$ to $M = 12$ are first solved (fig. S9). The mean value of ΔO_c increases slowly from 0 to ~ 0.33π as the channel number increases. This is because the least-squares solution requires more perturbations to fulfill Eq. 1 when M becomes larger. We have also swept the value of r from 0 to 1, and the calculated correlation matrices for each scenario are shown in fig. S11. It is noteworthy that because of the random nature of ΔO_n, the correlation matrices vary from time to time, even when the same level of ΔO_n is applied. To prevent fluctuation in the results, we take the statistical average of 10 correlation matrices. Lastly, to evaluate the multiplexing capacity, we follow a threshold value of 0.8 (*47*) for the correlation coefficient, resulting in the phase diagram shown in Fig. 3A. The examples that meet the threshold requirements (diagonal terms larger than 0.8 and nondiagonal terms less than 0.2 in this study) are marked in red (Phase I). By contrast, the rest (Phase II, Phase III, and Phase IV) cannot meet the requirements. When the noncorrelated noise is too small, the green region (Phase II, nondiagonal terms larger than 0.2) shows that the crosstalk is too strong. When the noncorrelated noise is too strong, the blue area (Phase III, diagonal terms less than 0.8) indicates that the patterns in the targeted channels have low intensity. We can see that the new upper limit is ~11 with $r = 0.5$. The upper limit might be increased further by relieving the threshold conditions (fig. S12). Figure 3, B and C, shows the optical and SEM micrographs of the sample for $M = 11$. Figure 3D presents the multiplexed holographic images measured in our experiment. By changing the polarization angles of incident light from 0° to 163.63° in the step of 16.36° each, 11 different holographic images are generated from the same metasurface. Despite some background noise, we can recognize all the designed Greek letters, including α, β, γ, δ, ρ, θ, λ, ψ, π, ε, and σ, demonstrating excellent performance of polarization multiplexing design in the new upper limit. The experimental results agree very well with the simulations shown in fig. S13. In addition to holograms, we expect that our design methodology can be applied to other metadevices such as metalenses. The key is to choose the appropriate parameters as the figure of merit and find the phase diagram for the specific applications (details shown in supplementary note 8).

Furthermore, our polarization multiplexing strategy based on noise engineering can be combined with other multiplexing methods, such as position multiplexing (fig. S14) and OAM multiplexing (fig. S15), to boost the information-encoding capacity. As in the last example, nine linear polarization channels (0°, 20°, 40°, 60°, 80°, 100°, 120°, 140°, 160°) are chosen, and each channel contains four

Fig. 4. Experimental demonstration of the holographic keyboard. (**A**) Optical and (**B**) SEM micrograph of the fabricated sample with simultaneously polarization- and position-multiplexed design. The scale bars are 50 μm and 0.4 μm, respectively. (**C**) Schematic and (**D**) measured results for the performance of the holographic keyboard pattern. Here we choose nine different polarization channels covering from 0° to 160°. Four holographic images are simultaneously generated at different planes away from the metasurface for each polarization channel. The locations of the planes are z_1 = 330 μm, z_2 = 430 μm, z_3 = 570 μm, and z_4 = 830 μm. As a result, 36 holographic images can be generated to form a typical keyboard pattern.

different holographic images at the planes 330, 430, 570, and 830 μm away from the metasurface (Fig. 4). The device is 330 μm by 330 μm in size. The optical and SEM micrographs of the metasurface are shown in Fig. 4, A and B. The target holographic images for the 36 channels at the wavelength of 700 nm are 26 letters and 10 Arabic digits, resulting in a typical keyboard pattern, as seen in the dashed region of Fig. 4C. Figure 4D depicts the measured results from the constructed metasurface, which create a total of 36 separate holographic images and match the design well. To the best of our knowledge, this is the largest capacity reported in metasurfaces with polarization and position multiplexing design, and it can be further improved by OAM multiplexing, wavelength multiplexing, angle multiplexing, and other techniques. The design combining noise engineering and OAM multiplexing is presented in supplementary note 9.

Concluding remarks

To summarize, we break the polarization multiplexing limit of metasurfaces with engineered noise in the visible region. It is expected that the capacity of traditional optical communication systems (e.g., wavelength multiplexing) and information storage systems (e.g., polarization multiplexing) can be further boosted with more parallel channels by using our approach. Furthermore, although we focus on metadevices operating in the visible frequencies, this design strategy can be readily applied to infrared, terahertz, or microwave frequencies. It opens a new pathway to enhance parallel processing, reduce cross-talk between channels, and increase the storage capacity in optical communication, optical encryption, and information storage systems.

REFERENCES AND NOTES

1. N. Yu *et al*., *Science* **334**, 333–337 (2011).
2. X. Ni, N. K. Emani, A. V. Kildishev, A. Boltasseva, V. M. Shalaev, *Science* **335**, 427–427 (2012).
3. S. Sun *et al*., *Nat. Mater.* **11**, 426–431 (2012).
4. L. Huang *et al*., *Nano Lett.* **12**, 5750–5755 (2012).
5. S. Chen, Z. Li, W. Liu, H. Cheng, J. Tian, *Adv. Mater.* **31**, e1802458 (2019).
6. Q. Wang *et al*., *ACS Photonics* **5**, 599–606 (2017).
7. J. N. Wang *et al*., *Small* **17**, e2101282 (2021).
8. Z. L. Deng *et al*., *Nano Lett.* **18**, 2885–2892 (2018).
9. Z. J. Wang *et al*., *ACS Photonics* **3**, 2096–2101 (2016).
10. Y. Zhao, M. A. Belkin, A. Alù, *Nat. Commun.* **3**, 870 (2012).
11. D. Lin, P. Fan, E. Hasman, M. L. Brongersma, *Science* **345**, 298–302 (2014).
12. M. I. Shalaev *et al*., *Nano Lett.* **15**, 6261–6266 (2015).
13. G. Zheng *et al*., *Nat. Nanotechnol.* **10**, 308–312 (2015).
14. M. Khorasaninejad *et al*., *Science* **352**, 1190–1194 (2016).
15. S. Wang *et al*., *Nat. Nanotechnol.* **13**, 227–232 (2018).
16. W. T. Chen, A. Y. Zhu, J. Sisler, Z. Bharwani, F. Capasso, *Nat. Commun.* **10**, 355 (2019).
17. R. H. Fan, B. Xiong, R. W. Peng, M. Wang, *Adv. Mater.* **32**, e1904646 (2020).
18. B. Wang *et al*., *Nano Lett.* **16**, 5235–5240 (2016).
19. B. Xiong *et al*., *Adv. Mater.* **33**, e2005864 (2021).
20. S. M. Kamali *et al*., *Phys. Rev. X* **7**, 041056 (2017).
21. X. Y. Fang, H. R. Ren, M. Gu, *Nat. Photonics* **14**, 102–108 (2020).
22. F. Z. Shu *et al*., *Laser Photonics Rev.* **15**, 2100155 (2021).
23. L. Li *et al*., *Nat. Commun.* **8**, 197 (2017).
24. M. Born, E. Wolf, *Principles of Optics* (Pergamon, ed. 6, 1980).
25. N. K. Grady *et al*., *Science* **340**, 1304–1307 (2013).
26. Y. J. Gao *et al*., *Phys. Rev. X* **10**, 031035 (2020).
27. E. Arbabi, S. M. Kamali, A. Arbabi, A. Faraon, *ACS Photonics* **6**, 2712–2718 (2019).
28. A. Arbabi, Y. Horie, M. Bagheri, A. Faraon, *Nat. Nanotechnol.* **10**, 937–943 (2015).
29. F. Ding, R. Deshpande, S. I. Bozhevolnyi, *Light Sci. Appl.* **7**, 17178 (2018).
30. J. Li *et al*., *Adv. Mater.* **33**, e2007507 (2021).
31. Z. L. Li *et al*., *Laser Photonics Rev.* **14**, 2000032 (2020).
32. Z. Li *et al*., *Opt. Express* **29**, 134–144 (2021).
33. Y. Bao, L. Wen, Q. Chen, C. W. Qiu, B. Li, *Sci. Adv.* **7**, eabh0365 (2021).
34. D. Wen *et al*., *Nat. Commun.* **6**, 8241 (2015).
35. F. Zhang, M. B. Pu, J. Luo, H. L. Yu, X. G. Luo, *Opto-Electron. Eng.* **44**, 319–325 (2017).
36. J. P. Balthasar Mueller, N. A. Rubin, R. C. Devlin, B. Groever, F. Capasso, *Phys. Rev. Lett.* **118**, 113901 (2017).
37. R. Zhao *et al*., *Light Sci. Appl.* **7**, 95 (2018).
38. H. Zhou *et al*., *ACS Nano* **14**, 5553–5559 (2020).
39. D. Zhu, Z. Liu, L. Raju, A. S. Kim, W. Cai, *ACS Nano* **15**, 2318–2326 (2021).
40. W. Ma *et al*., *Adv. Mater.* **34**, e2110022 (2022).
41. K. Hoffman, R. Kunze, *Linear Algebra*, Prentice-Hall, ed. 2 (1971).
42. A. E. Gamal, Y. H. Kim, *Network Information Theory*, Cambridge University Press (2011).
43. S. Ihara, *Information Theory for Continuous Systems*, World Scientific (1993).
44. Z. Shi *et al*., *Nano Lett.* **18**, 2420–2427 (2018).
45. M. D. Huntington, L. J. Lauhon, T. W. Odom, *Nano Lett.* **14**, 7195–7200 (2014).
46. G. Situ, J. J. Zhang, *J. Opt. A, Pure Appl. Opt.* **8**, 391–397 (2006).
47. Q. S. Wei, L. L. Huang, X. W. Li, J. Liu, Y. T. Wang, *Adv. Opt. Mater.* **5**, 1700434 (2017).

ACKNOWLEDGMENTS

Funding: R.P. and M.W. acknowledge financial support from the National Key R&D Program of China (grant nos. 2022YFA1404303 and 2020YFA0211300) and the National Natural Science Foundation of China (grants nos.12234010, 61975078, and 11974177). Yongmin Liu acknowledges financial support from the National Science Foundation (ECCS-1916839, ECCS-2136168, and DMR-2202268).
Author contributions: R.P., B.X., Yongmin Liu, Y.X., and M.W. conceived this work. B.X., Y.X., and L.D. contributed to the theoretical design; B.X., Yu Liu, and C.-W.C. fabricated the samples with the assistance of J.-N.W.; B.X. and Yu Liu performed the optical experiments; B.X., Y.X., L.D., R.P., Yongmin Liu, M.W., and Y. Lai contributed to the data analysis and discussion. R.P., Yongmin Liu, and M.W. directed and supervised the research. B.X., Y.X., L.D., Yongmin Liu, R.P., and M.W. drafted and finalized the manuscript. All authors revised the manuscript. **Competing interests:** The authors declare that they have no competing interests. **Data and materials availability:** All data needed to evaluate the conclusions in the paper are present in the main text and supplementary materials.
License information: Copyright © 2023 the authors, some rights reserved; exclusive licensee American Association for the Advancement of Science. No claim to original US government works. https://www.science.org/about/science-licenses-journal-article-reuse

SUPPLEMENTARY MATERIALS

science.org/doi/10.1126/science.ade5140
Materials and Methods
Supplementary Text
Figs. S1 to S15
References (*48*)

Submitted 21 August 2022; accepted 16 December 2022
10.1126/science.ade5140